

Selective CO Electroreduction to Multicarbon Oxygenates Over Atomically Dispersed Cu–Ag Sites in Alkaline Membrane Electrode Assembly Electrolyzer

Xinhui Guo⁺, Tianfu Liu⁺, Yanpeng Song, Rongtan Li, Pengfei Wei,^{*} Ziqi Liao, Zichao Wu, Dunfeng Gao, Qiang Fu, Guoxiong Wang,^{*} and Xinhe Bao

Abstract: Electrochemical carbon monoxide reduction reaction (CORR) to produce multicarbon (C₂₊) oxygenates using renewable electricity is a promising carbon utilization pathway. However, the performance of this process suffers from low C₂₊ oxygenates selectivity and insufficient current density. Here, we employed a Cu–Ag bimetallic strategy to enhance the selectivity of C₂₊ oxygenates from CORR in alkaline membrane electrode assembly electrolyzer at ampere-level current densities. The Cu–Ag catalysts prepared by magnetron sputtering feature atomically dispersed Cu–Ag sites on the catalyst surface, which are key to promoting the formation of C₂₊ oxygenates. Increasing Ag content favors C₂₊ oxygenates formation while inhibiting ethylene production. The optimized Cu₂Ag catalyst achieved Faradaic efficiency of 71.4% for C₂₊ oxygenates at 2.5 A cm^{−2}. In situ spectroscopy and density functional theory calculations revealed that atomically dispersed Cu–Ag sites on the catalyst surface promote the dissociation of *COCOH to *CCO, thus favoring C₂₊ oxygenates formation.

Introduction

In recent years, electrochemical CO reduction reaction (CORR) has demonstrated significant potential by producing multicarbon (C₂₊) fuels and chemicals such as ethylene, ethanol, acetic acid, and n-propanol.^[1–3] Compared to the earlier-studied electrochemical CO₂ reduction reaction,^[4–6] CORR offers several advantages, including higher current density (>1 A cm^{−2}), higher single-pass conversion (>80%, as CO does not react with the electrolyte to form carbonates),

higher Faradaic efficiency (FE) for C₂₊ products (>90%).^[7–10] Among the CORR products, C₂₊ oxygenates, such as ethanol and acetic acid, stand out due to their high atom utilization efficiency, high volumetric energy density, and convenience to transport.^[11,12] Currently, the annual production of ethanol and acetic acid has reached 77 and 18 Mt yr^{−1}, with prices of 650 and 800 USD t^{−1}, respectively.^[13] However, most reported CORR exhibits either low FEs of C₂₊ oxygenates (<70%) or insufficient current densities (<1 A cm^{−2}).^[9,14–16] Therefore, enhancing the selectivity of C₂₊ oxygenates at ampere-level current densities is of significant importance.

Over Cu-based catalysts, the byproducts of C₂₊ oxygenates include H₂ and ethylene. By constructing efficient three-phase interfaces, such as hydrophilic-hydrophobic modulation, it is possible to effectively suppress the FE of H₂ to less than 10% at ampere-level current densities.^[17,18] However, suppressing the generation of ethylene requires the regulation of the directed conversion of C₂ intermediates.^[2] Recent studies reported that the conversion of the key intermediate *COCOH is a crucial step in determining C₂ selectivity.^[19] Hydrogenation of *COCOH to form *COHCOH favors ethylene production, while its dissociation to form *CCO promotes the generation of ethanol and acetic acid. The adsorption energy of intermediates is strongly dependent on the structure of the adsorption site.^[16,20–22] For instance, it has been reported that isolated Cu sites lead to nearly monodentate adsorption of C₂ intermediates, which results in the formation of acetic acid.^[16]

Herein, we investigate the structure-performance relationship of Cu–Ag bimetallic catalysts in an alkaline membrane electrode electrolyzer (MEA) under ampere-level current densities (0.5–3.5 A cm^{−2}). we attempt to disperse the

[*] X. Guo⁺, Dr. T. Liu⁺, Y. Song, Dr. R. Li, Dr. P. Wei, Z. Liao, Z. Wu, Prof. Dr. D. Gao, Prof. Dr. Q. Fu, Prof. Dr. G. Wang, Prof. Dr. X. Bao
 State Key Laboratory of Catalysis, Dalian National Laboratory for Clean Energy, iChEM (Collaborative Innovation Center of Chemistry for Energy Materials), Dalian Institute of Chemical Physics, Chinese Academy of Sciences, Dalian 116023, China

E-mail: weipengfei@dicp.ac.cn
 wanggx@dicp.ac.cn
 wangguoxiong@fudan.edu.cn

Prof. Dr. G. Wang
 Department of Chemistry, Shanghai Key Laboratory of Electrochemical and Thermochemical Conversion for Resources Recycling, iChEM (Collaborative Innovation Center of Chemistry for Energy Materials), State Key Laboratory of Porous Materials for Separation and Conversion, Fudan University, Shanghai 200438, China

X. Guo⁺, Z. Liao, Z. Wu
 University of Chinese Academy of Sciences, Beijing 100049, China

Y. Song
 Department of Chemical Physics, University of Science and Technology of China, Hefei 230026, China

[†] Both authors contributed equally to this work.

Additional supporting information can be found online in the Supporting Information section

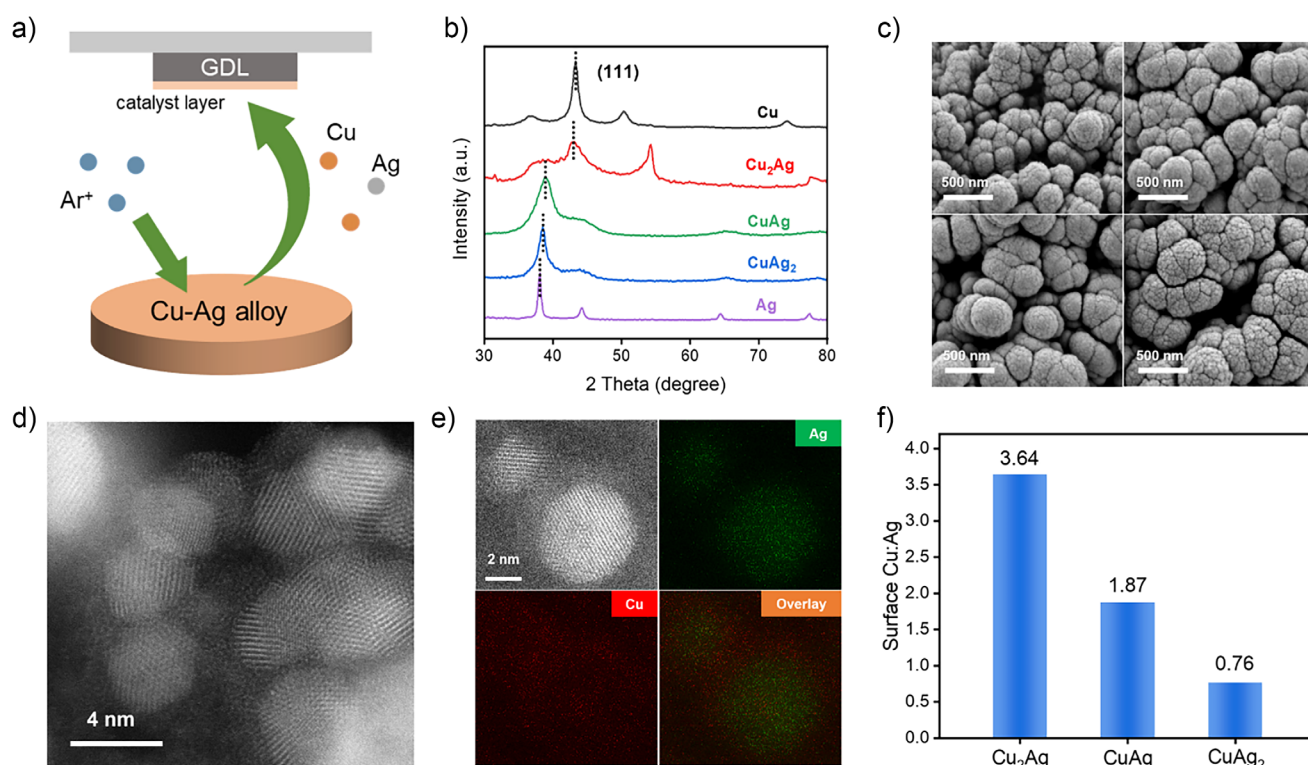


Figure 1. a) Schematic diagram of the magnetron sputtering process. b) GIXRD pattern of magnetron-sputtered Cu and Cu–Ag catalysts. c) SEM images of magnetron-sputtered Cu and Cu–Ag catalysts (top left: Cu; top right: Cu₂Ag; bottom left: CuAg; bottom right: CuAg₂). d) Aberration-corrected HAADF-STEM images of Cu₂Ag catalyst. e) HAADF-STEM image and EDS elemental maps of Cu₂Ag catalyst. f) Surface Cu/Ag ratio of different catalysts determined by XPS.

surface Cu sites by introducing Ag, a metal with weaker adsorption capacity for carbon species, thereby regulating the adsorption of C₂ intermediates on the catalyst surface. Atomically dispersed Cu–Ag sites are beneficial for the formation of C₂₊ oxygenates, and increasing the Ag content can enhance the selectivity of C₂₊ oxygenates. In situ spectroscopy characterizations and density functional theory (DFT) calculations show that the addition of Ag in sputtered Cu–Ag catalysts plays a role in dispersing Cu adsorption sites, which suppresses the hydrogenation of *COCOH to *COHCOH, a key intermediate for ethylene, while promoting the *OH cleavage of *COCOH toward *COO, thereby enhancing the selectivity of C₂₊ oxygenates.

Results and Discussion

A series of Cu–Ag bimetallic catalysts with different Cu/Ag ratios were prepared using magnetron sputtering (Figure 1a).^[23] The catalysts were denoted as Cu, Cu₂Ag, CuAg, CuAg₂, and Ag based on the target compositions. Under the same sputtering parameters, the Cu content in the gas diffusion electrodes loaded with Cu, Cu₂Ag, CuAg, and CuAg₂ catalysts was similar (Table S1). The double-layer capacitance measurements indicate that the four catalysts exhibit similar electrochemically surface active areas (ECSAs) (Figures S1 and S2). Inductively coupled plasma-optical emission spectrometry (ICP-OES) results indicate that

the Cu/Ag atomic ratios in the Cu₂Ag, CuAg, and CuAg₂ catalysts are 1.989, 0.980, and 0.498, respectively (Table S2), in consistent with the proportions in the target materials. As shown in Figure 1b, the (111) crystal plane 2θ peaks of magnetron-sputtered Cu, Cu₂Ag, CuAg, CuAg₂, and Ag catalysts in grazing incidence X-ray diffraction (GIXRD) pattern are located at 43.3°, 42.8°, 38.9°, 38.5°, and 38.1°. The (111) crystal plane peak of magnetron-sputtered Cu₂Ag, CuAg, and CuAg₂ catalysts is positioned between the (111) crystal plane peaks of Cu and Ag, suggesting that the catalyst primarily exists as a miscible Cu–Ag phase.

The morphological consistency and surface uniformity of the magnetron-sputtered catalysts were validated through electron microscopy imaging. Figure 1c shows scanning electron microscope (SEM) images of as-prepared magnetron-sputtered Cu, Cu₂Ag, CuAg, and CuAg₂ catalysts on gas diffusion layer, respectively, which exhibit similar morphology. SEM images of these magnetron-sputtered catalysts after CORR at 1 A cm^{−2} (Figure S3) show that the morphology remains unchanged. Cross-sectional SEM images of the gas diffusion electrodes (Figure S4) indicate that these four catalysts are uniformly distributed on the gas diffusion layer and exhibit similar thicknesses. High-angle annular dark field scanning transmission electron microscopy (HAADF-STEM) images of Cu₂Ag catalyst scraped off from gas diffusion layer (Figure 1d) show tiny sizes of approximately 3 nm. Energy dispersive spectroscopy (EDS) maps of Cu and Ag elements (Figure 1e) reveal that Ag mainly distribute at

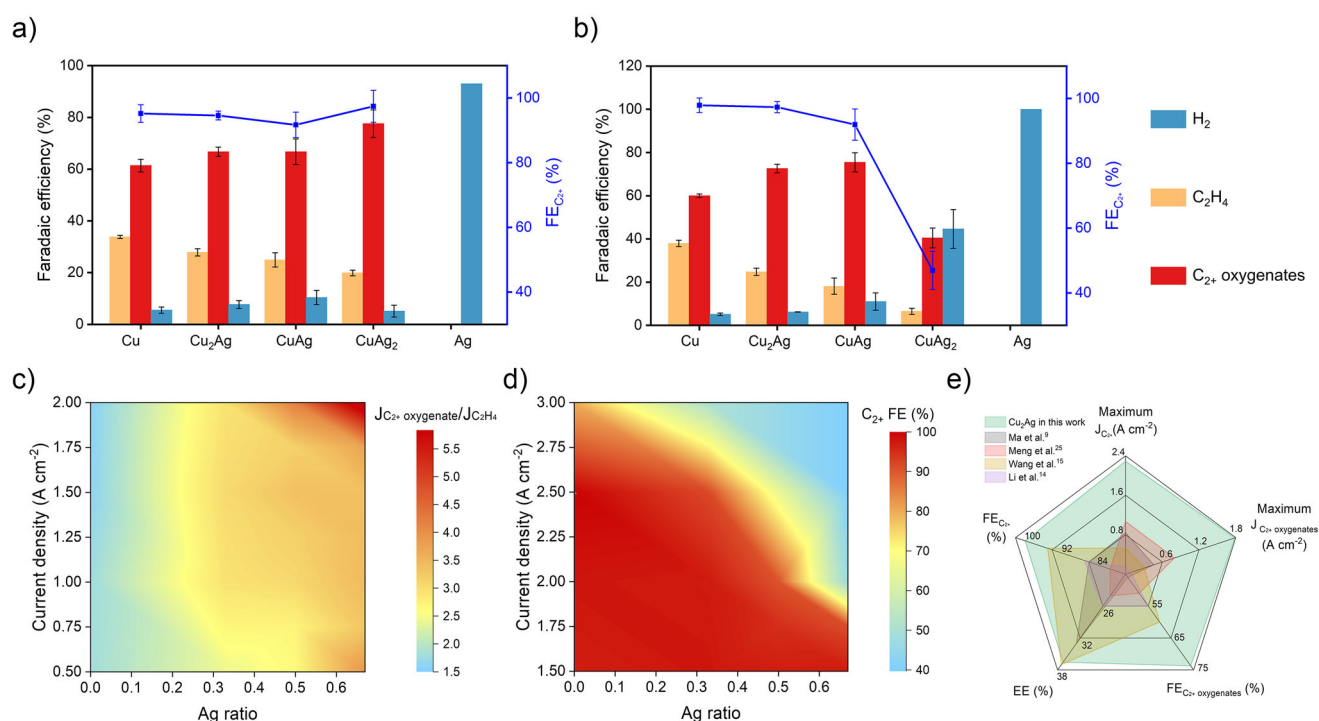


Figure 2. FEs of C_{2+} oxygenates, ethylene, and H_2 and cell voltages over magnetron-sputtered Cu and Cu–Ag catalysts at a) 0.5 A cm^{-2} and b) 2 A cm^{-2} . 2D heatmap for c) partial current density ratio of C_{2+} oxygenates and ethylene and d) FEs of total C_{2+} products over magnetron-sputtered catalysts with different Ag ratios at different current densities. e) Comparison of the performance metrics with the literature benchmarks for CO_2/CO -to- C_{2+} oxygenates conversion in alkaline MEA electrolyzer. The error bars represent standard error of the mean and are made based on three independent and identical measurements.

the inner layer, while Cu mainly distribute at the outer layer of the nanoparticle, indicative of a Cu surface segregation at the CuAg bimetallic particle. The HAADF-STEM image and corresponding EDS element maps of aged Cu_2Ag catalyst (Figures S4 and S6) are consistent with those of the fresh Cu_2Ag catalyst (Figure 1d,e), indicating that the Cu surface-segregated ultrasmall alloy nanoparticles are maintained during CORR. The elemental content on the catalyst surface was determined by X-ray photoelectron spectroscopy (XPS) of Cu 2p and Ag 3d (Table S3). As shown in Figure 1e, the Cu/Ag atomic ratios for Cu_2Ag , CuAg, and $CuAg_2$ catalysts are 3.64, 1.87, and 0.76, respectively, which are higher than the bulk phase ratios and consistent with the result of Cu surface segregation.

CO electrolysis performance measurements of these catalysts were conducted in an alkaline MEA electrolyzer with a geometric electrode area of 4 cm^2 that was previously reported by our group.^[24] The details of electrochemical performance measurements and product analysis are provided in the Experimental Procedures Section in Supporting Information. The detailed FEs of various CO electrolysis products and cell voltages data as a function of applied current densities over Cu, Cu_2Ag , CuAg, $CuAg_2$, and Ag catalysts, are provided in Figure S7. At 0.5 A cm^{-2} (Figure 2a), all these catalysts can efficiently inhibit hydrogen evolution reaction (HER) and promote C–C coupling (C_{2+} FE > 90%), with the main competitive product for C_{2+} oxygenates being C_2H_4 . With an increase of Ag content, FE of C_{2+} oxygenates

increase from 61.4% over Cu to 77.6% over $CuAg_2$, implying the addition of Ag facilitates the formation of C_{2+} oxygenates while simultaneously inhibiting ethylene generation. However, at a higher current density of 2 A cm^{-2} (Figure 2b), HER has begun to emerge as a dominant side reaction. The FE of H_2 sharply increases with an increase in the proportion of Ag, causing the FE of total C_{2+} products decrease from 97.9% over Cu catalyst to 46.9% over $CuAg_2$ catalyst. To better gauge the impact of Ag on the distribution of C_{2+} products, we analyzed the ratio of C_{2+} oxygenates and C_2H_4 as a function of Cu/Ag ratio and current density (Figure 2c). With an increase of Ag proportion, the ratio of partial current densities for C_{2+} oxygenates to ethylene increases, which suggests that in the Cu–Ag miscible catalyst, a higher Ag content favors the directed conversion of C_2 intermediates into C_{2+} oxygenates rather than ethylene. Figure 2d shows FE of total C_{2+} products as a function of Cu/Ag ratio and current density. As the proportion of Ag increases, the formation of C_{2+} products becomes more difficult at high current densities. For example, Cu catalyst achieves C_{2+} FE greater than 78% within a current density of 3 A cm^{-2} and greater than 95% within 2.5 A cm^{-2} . In contrast, $CuAg_2$ catalyst only reaches C_{2+} FE of 46.9% at 2 A cm^{-2} . Furthermore, at the same cell voltage, the ECSA-normalized partial current density for C_{2+} products decreases with increasing Ag content (Figure S8), implying that excess Ag impairs catalytic performance. Among the various Cu–Ag catalysts, Cu_2Ag catalyst exhibits the highest energy efficiency of 27.1% for C_{2+} oxygenates

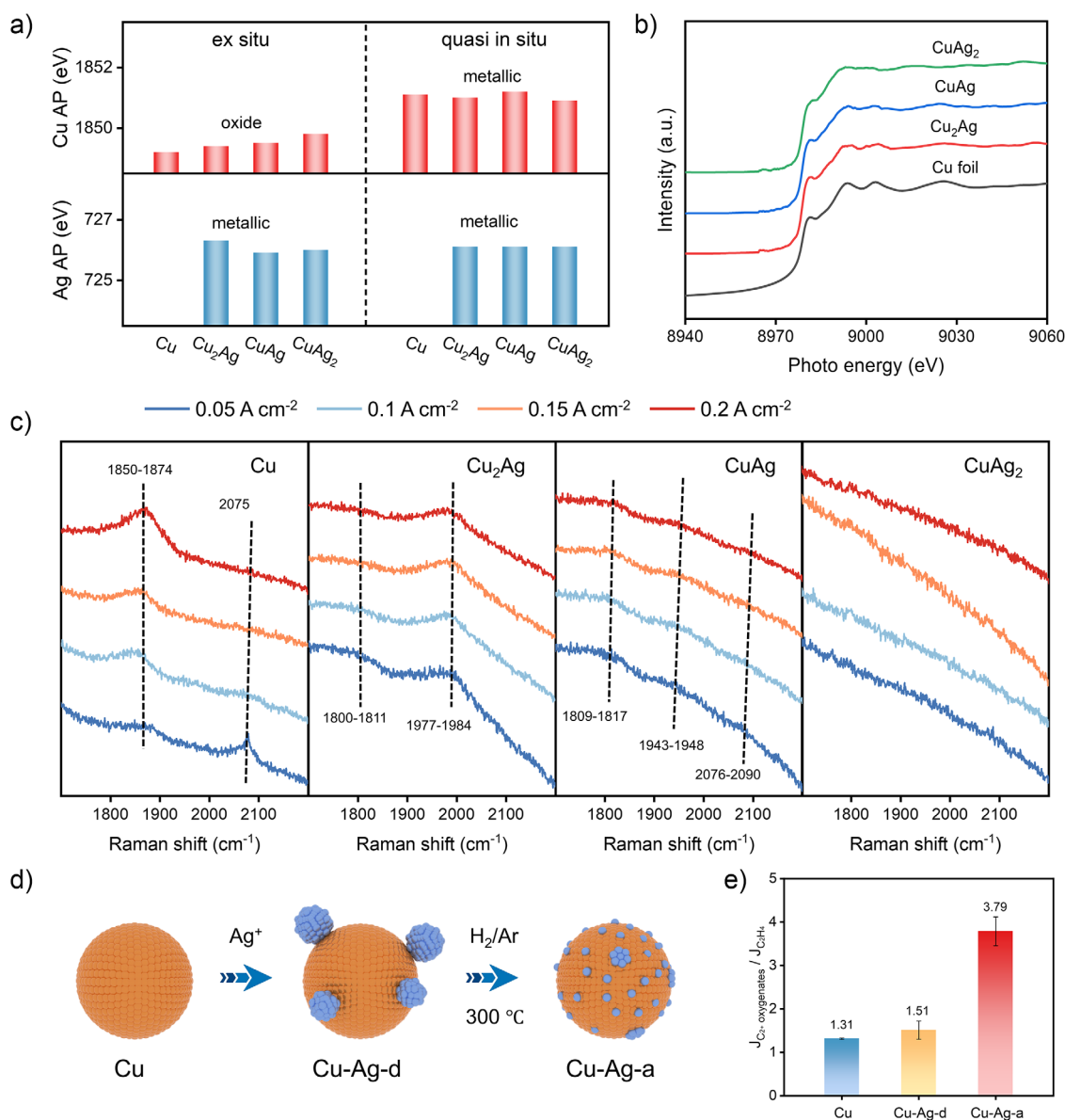


Figure 3. a) Deduced Cu and Ag Auger parameter from both ex situ and quasi in situ XPS data of different catalysts. b) Operando XANES spectra of Cu K edge measured in MEA cell at 1 A cm⁻². c) Operando Raman spectra measured in MEA cell within the wavenumber range of 1700–2200 cm⁻¹. d) Schematic illustration of Cu-Ag-d and Cu-Ag-a catalysts synthesis and site dispersity. e) Partial current density ratios of C₂₊ oxygenates to ethylene for Cu, Cu-Ag-d, and Cu-Ag-a catalysts at 2 A cm⁻². The error bars represent standard error of the mean and are made based on three independent and identical measurements.

at 1 A cm⁻² (Figure S9), and achieved the highest FE of 71.4% for oxygenates at 2.5 A cm⁻² (Figure S7b). Figure 3e compares CO electrolysis performances over Cu₂Ag catalyst with those of prior work,^[9,14,15,25] highlighting the excellent overall performance in this work.

To obtain information about the valence states of the catalysts during CORR, quasi in situ XPS measurements were performed on the catalyst after CORR without air exposure. The Auger parameters deduced from XPS spectra (Figures S10–S16) can be used to determine the valence states of Cu and Ag (Table S4).^[26,27] As shown in Figure 3a, the Cu Auger parameters acquired by ex situ XPS for Cu, Cu₂Ag, CuAg, and CuAg₂ catalysts are 1849.2, 1849.4, 1849.5, and

1849.8 eV, respectively, indicating that Cu primarily exists in the +1 oxidation state under air exposure. In contrast, the quasi in situ measurements reveal Cu Auger parameters of 1851.1, 1851.0, 1851.2, and 1850.9 eV for the four catalysts, respectively (Figure 3a and Table S5), suggesting that under the negative potential during CORR, Cu exists in its metallic state. The Ag Auger parameters obtained from both ex situ and quasi in situ measurements for different catalysts (Figure 3a and Table S6) ranges between 725.9 and 726.3 eV, close to 726.0 eV, indicating that Ag remains in its metallic state both before and during CORR.

The metallic state of Cu and Ag during CORR was further confirmed by Operando X-ray absorption near-edge

structure (XANES) spectra. Under open-circuit potential (OCP) conditions, the Cu K-edge of Cu₂Ag, CuAg, and CuAg₂ exhibited a noticeable shift to higher energy compared to that of Cu foil, indicating that Cu is in an oxidized state (Figure S17). After applying a current density of 1 A cm⁻², the Cu K-edge features of the catalysts become close to those of Cu foil (Figure 3b), suggesting that Cu is electrochemically reduced to its metallic state. The Ag K-edge features for catalysts under OCP and CORR conditions are close to those for Ag foil (Figure S18), indicating that Ag remains in the metallic state both before and after applying the current. Cu K-edge extended X-ray absorption fine structure (EXAFS) spectra (Figure S19) was fitted to obtain the Cu coordination information in the catalyst. The coordination numbers (CN) of Cu-Cu for the three samples measured at 1 A cm⁻² are 11.7, 10.2, and 6.1, respectively, while the CN of Cu-Ag are 1.5, 2.3, and 3.3, respectively (Table S7), which demonstrates the atomic inter-solubility of Cu and Ag in the bulk catalysts under CORR conditions.^[23]

To investigate the surface speciation of the catalysts and the adsorbed intermediates during CORR, Operando Raman spectroscopy was performed using a homemade MEA electrochemical cell (Figure S20). To verify that the data obtained under Raman spectroscopy measurement conditions accurately reflect the operational conditions, the morphology and product distribution of Cu₂Ag catalyst for Raman spectroscopy measurement was tested. The Cu₂Ag catalyst forms an island-like morphology (Figure S21), similar to the catalyst in alkaline MEA electrolyzer (Figure 1c). The product distribution measured in the Operando cell almost resembles that measured in alkaline MEA electrolyzer (Figures S7b and S22). At the Operando Raman spectra within the range of 240 to 700 cm⁻¹ (Figure S23), peaks at 390–401 cm⁻¹ and 532–547 cm⁻¹ were attributed to mixed copper oxide and hydroxide species (CuO_x/(OH)_y),^[28,29] which likely originated from surface-adsorbed OH⁻ species generated during the electrochemical reaction in the alkaline electrolyte (0.5 M KOH). A shoulder peak at 612–627 cm⁻¹ was assigned to Cu-O_{ad}.^[28,29] For the Ag-containing catalysts, new peaks around ~460 and ~650 cm⁻¹ likely related to OH⁻ were observed, which might be associated with the surface-exposed Ag in the catalysts.^[30,31] Figure 3c displays the Raman spectra of Cu, Cu₂Ag, CuAg, and CuAg₂ catalysts within the wavenumber range of 1700 to 2200 cm⁻¹. This range primarily involves the C≡O stretching vibrations of CO molecules adsorbed on the catalyst surface.^[32] The Cu catalyst exhibits two peaks at approximately 1850–1874 cm⁻¹ and 2075 cm⁻¹, corresponding to the bridge-site adsorption (*CO_{bridge}) and atop-site adsorption (*CO_{atop}) of CO on the Cu surface, respectively.^[32–34] At slightly higher current densities (>0.1 A cm⁻²), the intensity of *CO_{bridge} peak is significantly greater than that of *CO_{atop} peak, indicating that CO mainly adsorbs on the Cu surface in the bridge-site configuration during CORR. Cu₂Ag catalyst exhibits two peaks at approximately 1800–1811 and 1977–1984 cm⁻¹, while CuAg catalyst shows three peaks at around 1809–1817, 1943–1948, and 2076–2090 cm⁻¹, which indicates a significant change in surface adsorption sites, suggesting the formation of atomically dispersed Cu-Ag sites on the catalyst surface.^[23,35] With increasing Ag content, the intensity of the

C≡O stretching vibration peak gradually diminishes, which is also reflected in the weakening of the Cu-CO stretching mode observed at 314–320 cm⁻¹ (Figure S23).^[34,36] This attenuation may be attributed to the reduced CO surface coverage due to the weaker CO adsorption on Ag sites.

To verify the correlation between Cu-Ag atomic dispersion sites and the selectivity for C₂₊ oxygenates, the displacement Cu-Ag and annealing Cu-Ag catalysts (denoted as Cu-Ag-d and Cu-Ag-a, respectively) with different Cu-Ag dispersion were prepared according to a modified displacement approach^[10] based on Cu nanoparticles (Figure 3d and S24–S26). The XRD pattern indicates that Ag was successfully incorporated into Cu-Ag-d (Figure S24). HAADF-STEM images of both the as-prepared and post-electrolysis Cu-Ag-d catalyst and its corresponding EDS elemental maps (Figures S27 and S28), demonstrate that Ag and Cu are distributed in distinct nanoparticles, and no significant interdiffusion between Cu and Ag atoms was observed. After annealing in hydrogen atmosphere, the Cu-Ag-a particles underwent sintering and became larger in size (Figure S26b,c). Meanwhile, a high-contrast shell was observed on the surface of some particles, indicating that Ag atoms, which have a higher mass contrast, migrated and dispersed onto the surface of Cu particles under the influence of the reducing atmosphere. In the high-magnification HAADF-STEM images and corresponding EDS elemental maps of both as-prepared and post-electrolysis Cu-Ag-a catalysts (Figures S29 and S30), regions of Cu-Ag dispersion can be clearly observed, confirming the formation of atomically dispersed Cu-Ag sites in Cu-Ag-a catalyst. Quasi in situ XPS results reveal that both Cu and Ag in the Cu-Ag-d and Cu-Ag-a catalysts remain in the metallic state during CORR (Figures S31 and S32 and Table S4–S6), consistent with magnetron-sputtered Cu-Ag catalysts.

CO electrolysis performance measurements of Cu nanoparticles, Cu-Ag-d and Cu-Ag-a catalysts were conducted in an alkaline MEA electrolyzer, with the FEs of various CO electrolysis products and cell voltages displayed in Figure S33. Figure 3f compares the ratio of partial current densities for C₂₊ oxygenates to ethylene for these catalysts at 2 A cm⁻². The partial current density ratio of Cu-Ag-d catalyst is 1.51, similar to that of Cu nanoparticles at 1.31, indicating that isolated Ag nanoparticles have no significant effect on the distribution of C₂₊ products. While the partial current ratio of C₂₊ oxygenates to ethylene increases to 3.79 in Cu-Ag-a catalyst, suggesting that the formation of atomically dispersed Cu-Ag sites is a key factor in enhancing the selectivity of C₂₊ oxygenates. The Cu-Ag-a catalyst achieves an energy efficiency of 24.4% for C₂₊ oxygenates at 1 A cm⁻² (Figure S34), which is slightly lower than that of Cu₂Ag catalyst (27.1%). Considering that the Cu₂Ag catalyst has a significantly lower loading (0.25 mg cm⁻²) compared to Cu-Ag-a and Cu-Ag-d catalyst (1.5 mg cm⁻²) (Table S1), this highlights the technological superiority of Cu₂Ag catalyst in terms of cost-effectiveness and scalability.

On the basis of Operando Raman spectroscopy results, we employed DFT calculations to investigate the molecular-level mechanism by which Cu-Ag dispersion sites affect the performance of CORR. The *CO adsorption strength was

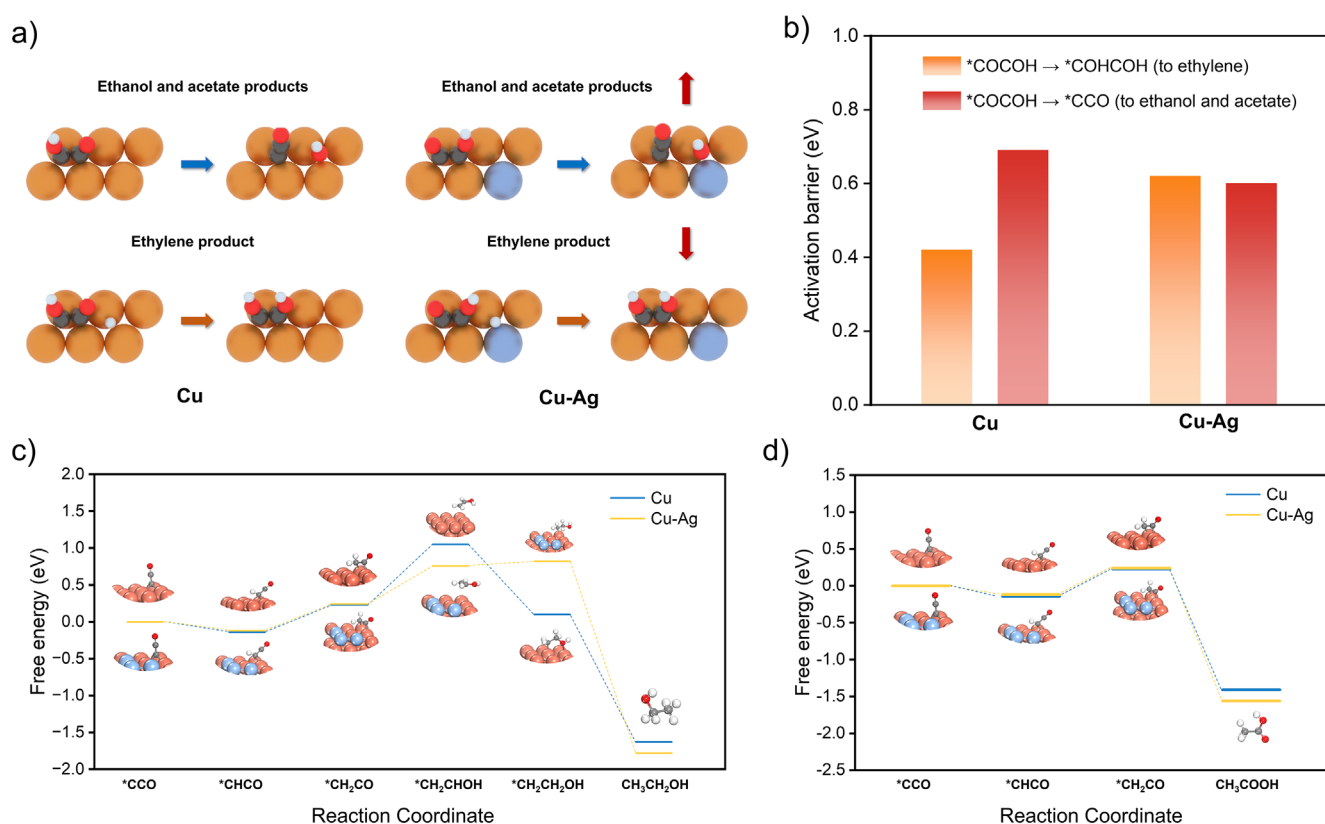


Figure 4. a) The schematic illustrations for the mechanism towards acetate and ethylene products. b) The activation barrier for *COCO_H to *COHCO_H or *CCO on Cu and Cu-Ag catalysts. The free energy profile for c) ethylene and d) acetate on Cu and Cu-Ag catalysts. Color code: red for oxygen, white for hydrogen, grey for carbon, orange for copper, and blue for silver.

calculated on Cu and Cu-Ag alloy surfaces with varying Ag contents (Cu/Ag = 8:1, 7:2, and 2:1). The average *CO adsorption energies were −0.88 eV for Cu, −0.62 eV for Cu₈Ag₁, −0.60 eV for Cu₇Ag₂, and −0.59 eV for Cu₂Ag₁ (Figure S35). These results reveal a progressive weakening of *CO adsorption with increasing Ag incorporation. This trend suggests that Ag incorporation weakens the *CO binding, which may lower the surface *CO coverage and thereby decrease the partial current density of total C₂₊ products.

To further understand the role of Ag in tuning C₂₊ products distribution, we examined the energy barrier for the transformation of *COCO_H, which has been identified as the key intermediate for selectivity of ethanol, acetate, and ethylene.^[19,37] The dissociation of −OH of *COCO_H leads to the formation of *CCO, which is further reduced to ethanol and acetate, while the hydrogenation of *COCO_H to *COHCO_H leads to ethylene formation. We constructed Cu and Cu-Ag models for investigation, as shown in Figure 4a, where an Ag atom was added adjacent to several Cu atoms. These Cu atoms together with the Ag atom served as the reactive active site for Cu-Ag. As shown in Figure 4b, the activation barrier of the formation of *COO and *COHCO_H clearly shows that the ethylene is favored on Cu, with a lower barrier of 0.42 eV for *COHCO_H formation compared to that of ethanol and acetate (*CCO with 0.69 eV). Interestingly, on Cu-Ag, the barrier for ethylene increases to 0.62 eV, while the acetate decreases to 0.60 eV. We can see that the selectivity

trend is reversed to favorable ethanol and acetate production with the doping of Ag on Cu. Ag makes the hydrogenation step of *COCO_H to *COHCO_H energetically challenging. In contrast, the *CCO intermediate is less influenced by Ag atom. The addition of Ag is effective in tuning the formation of key intermediates. Moreover, we studied the energetical profile from *COHCO_H to ethylene and *CCO to ethanol and acetate. The ethylene pathway is more facile on Cu with downhill trend, but more difficult on Cu-Ag with an uphill step of *CH₂CHOH to *CH₂CH (Figure S36). The incorporation of Ag significantly promotes ethanol formation by reducing the free energy increase associated with the key step CH₂CO to CH₂CHOH (Figure 4c). The acetate production is almost the same on Cu and Cu-Ag catalysts (Figure 4d). Therefore, both the kinetic and thermodynamic analysis indicate that ethylene is more facile to be generated on Cu catalyst, while ethanol and acetate production is more favored over Cu-Ag catalyst.

Conclusion

We systematically explored the potential of Cu-Ag catalysts for CO electroreduction to C₂₊ oxygenates in alkaline MEA electrolyzer. Cu-Ag catalysts synthesized via magnetron sputtering showed that a higher Ag content increases the FE ratio of C₂₊ oxygenates to ethylene, although an excessively high

Ag content is unfavorable for the formation of total C_{2+} products at high current densities. In situ spectroscopic analyses and performance comparisons of catalysts with different Cu–Ag dispersion indicate that the formation of surface Cu–Ag atomically dispersed sites is key to enhancing the selectivity for C_{2+} oxygenates. DFT calculations elucidated the critical role of Ag in disrupting Cu site continuity and altering intermediate adsorption configurations. This work provides an effective design strategy for regulating the selectivity of C_{2+} oxygenates, achieving FE of 71.4% for C_{2+} oxygenates at a current density of 2.5 A cm^{-2} .

Supporting Information

The authors have cited additional references within the Supporting Information.^[38–47]

Acknowledgements

This work was supported by the National Key R&D Program of China (2023YFA1508000), the National Natural Science Foundation of China (22125205, 22302204, 22321002, U24A20499, 22494711 and 22350710789), the Strategic Priority Research Program of the Chinese Academy of Sciences (XDB0600200), the Liaoning Binhai Laboratory (LBLF-2023–02), the Joint Fund of the Yulin University and the Dalian National Laboratory for Clean Energy (YLU-DNL Fund 2022008), the Fundamental Research Funds for the Central Universities (20720220008), the China Postdoctoral Science Foundation (2023M743429, 2023TQ0350), Postdoctoral Fellowship Program of CPSF (GZC20232588), and the Photon Science Center for Carbon Neutrality. The authors thank the Shanghai Synchrotron Radiation Facility of BL14W1 (31124.02.SSRF.BL14BW1) for the assistance on XAS measurements.

Conflict of Interests

The authors declare no conflict of interest.

Data Availability Statement

The data that support the findings of this study are available from the corresponding author upon reasonable request.

Keywords: CO electroreduction • Cu–Ag catalyst • Membrane electrode assembly • Multicarbon oxygenates

[1] M. Jouny, W. Luc, F. Jiao, *Nat. Catal.* **2018**, *1*, 748–755.

[2] W. Ma, X. He, W. Wang, S. Xie, Q. Zhang, Y. Wang, *Chem. Soc. Rev.* **2021**, *50*, 12897–12914.

[3] C. W. Li, J. Ciston, M. W. Kanan, *Nature* **2014**, *508*, 504–507.

[4] C.-T. Dinh, T. Burdyny, M. G. Kibria, A. Seifitokaldani, C. M. Gabardo, F. P. García de Arquer, A. Kiani, J. P. Edwards, P. De Luna, O. S. Bushuyev, C. Zou, R. Quintero-Bermudez, Y. Pang, D. Sinton, E. H. Sargent, *Science* **2018**, *360*, 783–787.

- [5] Y. Shi, M. Hou, J. Li, L. Li, Z. Zhang, *Acta Phys.-Chim. Sin.* **2022**, *38*, 2206020.
- [6] J. A. Rabinowitz, M. W. Kanan, *Nat. Commun.* **2020**, *11*, 5231.
- [7] X. Ding, J. Zhang, Y. Li, *eScience* **2023**, *3*, 100137.
- [8] H. Li, P. Wei, T. Liu, M. Li, C. Wang, R. Li, J. Ye, Z.-Y. Zhou, S.-G. Sun, Q. Fu, D. Gao, G. Wang, X. Bao, *Nat. Commun.* **2024**, *15*, 4603.
- [9] W. Ma, S. Xie, B. Zhang, X. He, X. Liu, B. Mei, F. Sun, Z. Jiang, L. Lin, Q. Zhang, B. Ren, G. Fu, X. Hu, Y. Wang, *Chem* **2023**, *9*, 2161–2177.
- [10] Y. Ji, Z. Chen, R. Wei, C. Yang, Y. Wang, J. Xu, H. Zhang, A. Guan, J. Chen, T.-K. Sham, J. Luo, Y. Yang, X. Xu, G. Zheng, *Nat. Catal.* **2022**, *5*, 251–258.
- [11] L. Ding, N. Zhu, Y. Hu, Z. Chen, P. Song, T. Sheng, Z. Wu, Y. Xiong, *Angew. Chem. Int. Ed.* **2022**, *61*, e202209268.
- [12] D. Zang, Q. Li, G. Dai, M. Zeng, Y. Huang, Y. Wei, *Appl. Catal., B* **2021**, *281*, 119426.
- [13] C. P. O'Brien, R. K. Miao, A. Shayesteh Zeraati, G. Lee, E. H. Sargent, D. Sinton, *Chem. Rev.* **2024**, *124*, 3648–3693.
- [14] J. Li, H. Xiong, X. Liu, D. Wu, D. Su, B. Xu, Q. Lu, *Nat. Commun.* **2023**, *14*, 698.
- [15] X. Wang, P. Ou, A. Ozden, S.-F. Hung, J. Tam, C. M. Gabardo, J. Y. Howe, J. Sisler, K. Bertens, F. P. García de Arquer, R. K. Miao, C. P. O'Brien, Z. Wang, J. Abed, A. S. Rasouli, M. Sun, A. H. Ip, D. Sinton, E. H. Sargent, *Nat. Energy* **2022**, *7*, 170–176.
- [16] J. Jin, J. Wicks, Q. Min, J. Li, Y. Hu, J. Ma, Y. Wang, Z. Jiang, Y. Xu, R. Lu, G. Si, P. Papangelakis, M. Shakouri, Q. Xiao, P. Ou, X. Wang, Z. Chen, W. Zhang, K. Yu, J. Song, X. Jiang, P. Qiu, Y. Lou, D. Wu, Y. Mao, A. Ozden, C. Wang, B. Y. Xia, X. Hu, V. P. Dravid, Y.-M. Yiu, T.-K. Sham, Z. Wang, D. Sinton, L. Mai, E. H. Sargent, *Nature* **2023**, *617*, 724–729.
- [17] J.-J. Lv, R. Yin, L. Zhou, J. Li, R. Kikas, T. Xu, Z.-J. Wang, H. Jin, X. Wang, S. Wang, *Angew. Chem. Int. Ed.* **2022**, *61*, e202207252.
- [18] P. Wei, D. Gao, T. Liu, H. Li, J. Sang, C. Wang, R. Cai, G. Wang, X. Bao, *Nat. Nanotechnol.* **2023**, *18*, 299–306.
- [19] J. Li, C. Li, J. Hou, W. Gao, X. Chang, Q. Lu, B. Xu, *J. Am. Chem. Soc.* **2022**, *144*, 20495–20506.
- [20] J. Li, A. Xu, F. Li, Z. Wang, C. Zou, C. M. Gabardo, Y. Wang, A. Ozden, Y. Xu, D.-H. Nam, Y. Lum, J. Wicks, B. Chen, Z. Wang, J. Chen, Y. Wen, T. Zhuang, M. Luo, X. Du, T.-K. Sham, B. Zhang, E. H. Sargent, D. Sinton, *Nat. Commun.* **2020**, *11*, 3685.
- [21] Y. Wang, Z. Wang, C.-T. Dinh, J. Li, A. Ozden, M. Golam Kibria, A. Seifitokaldani, C.-S. Tan, C. M. Gabardo, M. Luo, H. Zhou, F. Li, Y. Lum, C. McCallum, Y. Xu, M. Liu, A. Proppe, A. Johnston, P. Todorovic, T.-T. Zhuang, D. Sinton, S. O. Kelley, E. H. Sargent, *Nat. Catal.* **2020**, *3*, 98–106.
- [22] C. Du, J. P. Mills, A. G. Yohannes, W. Wei, L. Wang, S. Lu, J.-X. Lian, M. Wang, T. Guo, X. Wang, H. Zhou, C.-J. Sun, J. Z. Wen, B. Kendall, M. Couillard, H. Guo, Z. Tan, S. Siahrostami, Y. A. Wu, *Nat. Commun.* **2023**, *14*, 6142.
- [23] Y. C. Li, Z. Wang, T. Yuan, D.-H. Nam, M. Luo, J. Wicks, B. Chen, J. Li, F. Li, F. P. G. de Arquer, Y. Wang, C.-T. Dinh, O. Voznyy, D. Sinton, E. H. Sargent, *J. Am. Chem. Soc.* **2019**, *141*, 8584–8591.
- [24] P. Wei, H. Li, L. Lin, D. Gao, X. Zhang, H. Gong, G. Qing, R. Cai, G. Wang, X. Bao, *Sci. China Chem.* **2020**, *63*, 1711–1715.
- [25] N. Meng, Z. Wu, Y. Huang, J. Zhang, M. Chen, H. Ma, H. Li, S. Xi, M. Lin, W. Wu, S. Han, Y. Yu, Q.-H. Yang, B. Zhang, K. P. Loh, *Nat. Commun.* **2024**, *15*, 3892.
- [26] R. Li, X. Xu, B. Zhu, X.-Y. Li, Y. Ning, R. Mu, P. Du, M. Li, H. Wang, J. Liang, Y. Chen, Y. Gao, B. Yang, Q. Fu, X. Bao, *Nat. Commun.* **2021**, *12*, 1406.
- [27] G. Moretti, H. P. Beck, *Surf. Interface Anal.* **2022**, *54*, 803–812.
- [28] Y. Zhao, X. Chang, A. S. Malkani, X. Yang, L. Thompson, F. Jiao, B. Xu, *J. Am. Chem. Soc.* **2020**, *142*, 9735–9743.
- [29] X. Chang, Y. Zhao, B. Xu, *ACS Catal.* **2020**, *10*, 13737–13747.

- [30] M. Chen, D. Liu, Y. Chen, D. Liu, X. Du, J. Feng, P. Zhou, B. Zi, Q. Liu, K. H. Lo, S. Chen, S. Wang, W. F. Ip, H. Pan, *Appl. Mater. Today* **2022**, *26*, 101343.
- [31] N. Bodappa, M. Su, Y. Zhao, J.-B. Le, W.-M. Yang, P. Radjenovic, J.-C. Dong, J. Cheng, Z.-Q. Tian, J.-F. Li, *J. Am. Chem. Soc.* **2019**, *141*, 12192–12196.
- [32] C. M. Gunathunge, X. Li, J. Li, R. P. Hicks, V. J. Ovalle, M. M. Waegle, *J. Phys. Chem. C* **2017**, *121*, 12337–12344.
- [33] X. Wang, Y. Zhang, J. Shi, J. Cai, G. Liu, J. Tang, *J. Phys. Chem. C* **2023**, *127*, 13034–13043.
- [34] D. Zhong, Z.-J. Zhao, Q. Zhao, D. Cheng, B. Liu, G. Zhang, W. Deng, H. Dong, L. Zhang, J. Li, J. Li, J. Gong, *Angew. Chem. Int. Ed.* **2021**, *60*, 4879–4885.
- [35] J. Gao, H. Zhang, X. Guo, J. Luo, S. M. Zakeeruddin, D. Ren, M. Grätzel, *J. Am. Chem. Soc.* **2019**, *141*, 18704–18714.
- [36] Y. Zhao, X.-G. Zhang, N. Bodappa, W.-M. Yang, Q. Liang, P. M. Radjenovica, Y.-H. Wang, Y.-J. Zhang, J.-C. Dong, Z.-Q. Tian, J.-F. Li, *Energy Environ. Sci.* **2022**, *15*, 3968–3977.
- [37] P. Zhu, C. Xia, K. Jiang, G. Gao, X. Zhang, Y. Xia, Y. Lei, H. N. Alshareef, T. P. Senftle, H. Wang, *Proc. Nat. Acad. Sci.* **2021**, *118*, e2010868118.
- [38] H. Peng, Q. Li, M. Hu, L. Xiao, J. Lu, L. Zhuang, *J. Power Sources* **2018**, *390*, 165–167.
- [39] D. Briggs, *Handbook of X-ray photoelectron spectroscopy*, (Eds.: C. D. Wanger, W. M. Riggs, L. E. Davis, J. F. Moulder, G. E. Muilenberg), Perkin-Elmer Corp, Physical Electronics Division, Eden Prairie, Minnesota, USA **1979**, Vol. 3, pp. 1–190.
- [40] G. Kresse, J. Furthmüller, *Comput. Mater. Sci.* **1996**, *6*, 15–50.
- [41] G. Kresse, J. Furthmüller, *Phys. Rev. B* **1996**, *54*, 11169–11186.
- [42] B. Hammer, L. B. Hansen, J. K. Nørskov, *Phys. Rev. B* **1999**, *59*, 7413–7421.
- [43] Y. Zhang, W. Yang, *Phys. Rev. Lett.* **1998**, *80*, 890–890.
- [44] P. E. Blöchl, *Phys. Rev. B* **1994**, *50*, 17953–17979.
- [45] G. Kresse, D. Joubert, *Phys. Rev. B* **1999**, *59*, 1758–1775.
- [46] G. Henkelman, B. P. Uberuaga, H. Jónsson, *J. Chem. Phys.* **2000**, *113*, 9901–9904.
- [47] A. A. Peterson, F. Abild-Pedersen, F. Studt, J. Rossmeisl, J. K. Nørskov, *Energy Environ. Sci.* **2010**, *3*, 1311–1315.

Manuscript received: March 28, 2025

Revised manuscript received: April 25, 2025

Accepted manuscript online: May 06, 2025

Version of record online: ■■■■■

Research Article

CO Electroreduction

X. Guo, T. Liu, Y. Song, R. Li, P. Wei*,
Z. Liao, Z. Wu, D. Gao, Q. Fu, G. Wang*,
X. Bao ————— e202507062

Selective CO Electroreduction to
Multicarbon Oxygenates Over Atomically
Dispersed Cu–Ag Sites in Alkaline
Membrane Electrode Assembly
Electrolyzer

Atomically dispersed Cu–Ag sites on the catalyst surface promote the *OH cleavage of *COCOH toward *COO, thereby enhancing the selectivity of C₂₊ oxygenates from CO electroreduction. CO electrolysis over the optimized CuAg catalyst achieves a Faradaic efficiency of 71.4% for C₂₊ oxygenates at a current density of 2.5 A cm⁻² in alkaline membrane electrode assembly electrolyzer.

